International Journal of Plasticity 27 (2011) 688–706

Contents lists available at ScienceDirect

International Journal of Plasticity

journal homepage: www.elsevier.com/locate/ijplas

Mechanical response and texture evolution of AZ31 alloy at large strains for different strain rates and temperatures

Akhtar S. Khan [a], Amit Pandey [a,b,*], Thomas Gnäupel-Herold [c], Raja K. Mishra [d]

[a] Department of Mechanical Engineering, University of Maryland Baltimore County, MD 21250, USA
[b] Department of Mechanical Engineering, The Johns Hopkins University, Baltimore, MD 21218, USA
[c] NIST Center for Neutron Research, Gaithersburg, MD 20899-8562, USA
[d] General Motors Global R&D Center, Warren, MI 48090-9055, USA

ARTICLE INFO

Article history:
Received 22 November 2009
Received in final revised form 22 August 2010
Available online 9 September 2010

Keywords:
Magnesium (AZ31)
Tension/compression/simple shear
Strain rate
Texture
Neutron diffraction/EBSD

ABSTRACT

In order to study the behavior of material under finite deformation at various strain rates, the responses of AZ31 Mg sheet are measured under uniaxial (tension and compression) and multiaxial (simple shear) loadings along rolling direction (RD), 45° to rolling direction (DD), 90° to rolling direction (TD), and normal to the sheet (ND) to large strains. The material exhibits positive strain rate sensitivity (SRS) at room and elevated temperatures; the SRS is more pronounced at high temperatures and lower strain rates. The *r*-value of the material under tensile loading at room temperatures is higher in TD at lower strain rate. Texture measurements on several failed specimens are reported under tension and simple shear after finite plastic deformation of about 20% equivalent strain. The as-received material exhibits a strong fiber with equal fractions of grains having the *c*-axis slightly tilted away from the sheet normal towards both +RD and −RD. Pole figures obtained after tensile loading along the rolling direction (RD) show that the texture of the material strengthens even at low strains, with *c*-axis perpendicular to the sheet plane and prism planes lining up in a majority of grains. However, the tensile loading axis along TD does not lead to similar texture strengthening; the *c*-axis distribution appears to be virtually unchanged from the virgin state. The pole figures obtained after in-plane compression along RD brings the *c*-axes of the grains parallel to the loading direction. The pole figures after simple shear loading show that the *c*-axis rotates to lie on the sheet plane consistent with a compression axis 45° away on the sheet plane.

1. Introduction

Weight reduction of automobiles has emerged as one of the most attractive options for significant advances in both fuel efficiency and the resulting reduction in CO_2 emissions (Aghion et al., 2001). With increased efforts to bring the cost down, magnesium alloys are finding increasing use in the automotive field to take advantage of their high strength-to-weight ratio. In addition, magnesium alloys find use in biomedical application due to the good biocompatibility of Zn and Mn alloying additions to Mg (Zhang et al., 2009). The combination of poor formability at room temperature, high ductility at elevated temperatures, and asymmetric response of wrought Mg alloy under compression and tension (Hilditch et al., 2009) limit the use of magnesium alloys for widespread structural applications. It is of significant interest to study the thermo-mechanical

* Corresponding author at: Department of Mechanical Engineering, The Johns Hopkins University, Baltimore, MD 21218, USA. Tel.: +1 410 455 3301; fax: +1 410 455 1052.
E-mail addresses: khan@umbc.edu (A.S. Khan), dramitpandey@gmail.com (A. Pandey).

0749-6419/$ - see front matter © 2010 Elsevier Ltd. All rights reserved.
doi:10.1016/j.ijplas.2010.08.009

responses and deformation mechanisms at large strains and over the wide ranges of strain rates and temperatures to create guidelines for design and usage of Mg alloys in devices and applications.

In addition to the pioneering work of Backofen et al. (1964) and Reed-Hill (1973), recent works by Agnew et al. (2003), Staroselsky and Anand (2003), Nave and Barnett (2004), Brown et al. (2005), Jiang et al. (2007) and Proust et al. (2009) have provided experimental and modeling results on deformation of Mg alloys under different strain paths, strain rates and temperatures. According to the published data, basal slip $\{0\,0\,0\,1\}\langle 1\,1\,\bar{2}\,0\rangle$, prismatic slip $\{1\,0\,\bar{1}\,0\}\langle 1\,1\,\bar{2}\,0\rangle$, pyramidal-I slip $\{1\,0\,\bar{1}\,1\}\langle 1\,1\,\bar{2}\,0\rangle$, pyramidal-II $\{1\,0\,\bar{1}\,2\}\langle 1\,1\,\bar{2}\,3\rangle$, slip and twinning on pyramidal systems $\{1\,0\,\bar{1}\,2\}\langle\bar{1}\,0\,1\,1\rangle$ and $\{\bar{1}\,0\,1\,1\}\langle 1\,0\,\bar{1}\,2\rangle$, get activated at widely different critical stress levels during the deformation of AZ31 at room temperature. The low formability of Mg alloys at room temperature is because of the difficulty of having adequate basal and non- basal deformation mechanisms available to accommodate general deformation in three dimensions without premature fracture. At elevated temperatures, pyramidal-II (or $\langle c+a\rangle$) slip occurs at lower critical resolved shear stress (CRSS) and most Mg alloys, including AZ31, become quite formable (Agnew et al., 2001; Agnew and Duygulu, 2005). The crystallography of the twins and the accompanying lattice reorientation by extension and contraction twins has been well documented in the literature.

Lou et al. (2007) have pointed out that the forming of sheet metal predominantly involves the combination of bending and stretching – mainly in-plane loading conditions with much smaller through thickness stresses. Thus, in-plane deformation studies of sheet alloys are essential for forming applications. Recently, a comprehensive study on the evolution of yield surfaces was performed by Khan et al. (2009, 2010a,b) on Al alloys to study the forming and springback phenomenon. In the case of magnesium sheet alloys, the texture is such that the basal planes of the grains are parallel to the sheet surface; yield stress in tension is almost twice that of the in-plane compression. This has been shown to be due to the different deformation mechanisms in tension and compression of these textured sheets, in-plane compression activates twinning at low stresses whereas in-plane tensile stress cannot induce such twins (Reed-Hill, 1973; Reed-Hill and Abbaschian, 1994; Lou et al., 2007). Tensile loading normal to the sheet plane activates twinning at lower stress while compressive loading normal to the sheet plane does not activate twinning (Reed-Hill, 1973; Agnew et al., 2001; Staroselsky and Anand, 2003; Styczynski et al., 2004). In-plane stress–strain curves in compression exhibit an inflection hardening for moderate strains; for large strains, the stress–strain curves look similar to a tension stress–strain curve. As a result of the reorientation of the grains by nearly 90° (86° by extension twinning) following twinning under compressive loading. However, at high temperature the inflection hardening curve vanishes due to the activation of many slip systems with lower CRRS (Lou et al., 2007; Nobre et al., 2002; Yukutake et al., 2003; Nave and Barnett, 2004).

Agnew and Duygulu (2005) and Lou et al. (2007) have studied the anisotropy and hardening of AZ31 alloy under tension and showed that the deformation was initially due to the basal slip and gradually shift towards non-basal slip due to an increase in flow stress at room temperature. Jiang et al., (2007) studied the evolution of twinning under uniaxial and ring hoop tension loading at elevated temperature and concluded that the effect of twinning was more significant due to flow stress than the grain size. Jain et al., 2008 have reported that the strain anisotropy (r-value) did not change significantly with grain size at room temperature. Proust et al., 2009 have shown that most of the deformation in tensile loading at room temperature was due to basal $\langle a\rangle$ and prismatic $\langle a\rangle$ slip. High temperature tension experiments were performed by Abu-Farha and Khraisheh (2007), Del Valle et al. (2005), Watanabe et al. (2001) and Liu and Wu (2006) at low strain rates to study the superplasticity (very high ductility) of AZ31 alloy. In these experiments, loading was performed along in-plane direction on sheet metal using dog-bone specimens. Similar studies on cylindrical specimens of AZ31 alloy have also been reported by Yi et al. (2006) along with X-ray texture data to investigate the bulk properties of superplastic AZ31 alloy. These studies have identified the role of grain boundary sliding in high temperature deformation.

In plane uniaxial compression experiments are difficult to perform because of the limitation of buckling, especially at elevated temperatures. Uniaxial and biaxial compression experiments on sheet metal were first performed by Tozawa (1978) at room temperatures by gluing the sheets. Boger et al. (2005) developed an approach to avoid the limitations of existing designs for in-plane compression where a modified dog-bone specimen was used. Lou et al. (2007) extended this test method to perform uniaxial compression and cyclic tension-compression experiments; two flat steel plates and a hydraulic cylinder system were used to stabilize the sheet sample. As a consequence, the actual stress–strain curves were obtained after making corrections for friction between sample surfaces and supporting plates and biaxial stress state. Proust et al. (2009) also performed in plane compression and through thickness compression experiments on AZ31 sheet alloy at room temperatures and showed that the hardening rate associated with the former was due to twinning whereas in the later case the material deformed via basal $\langle a\rangle$ and pyramidal $\langle c+a\rangle$ slip. Uniaxial compression experiments performed by Jain and Agnew (2007) at elevated temperatures proved that the yield point during in-plane compression is insensitive to temperature up to 200 °C and athermal mechanisms were responsible for yielding. Cylindrical specimens have been used by Choi et al. (2007), Yi et al. (2006), Chino et al. (2008), Al-Samman and Gottstein (2008), Helis et al. (2006) and Jiang et al. (2008) to obtain the compression response for finite deformation and the results have confirmed the findings for sheet specimens. The in-plane simple shear test has proved to be very efficient for the evaluation of mechanical properties of sheet materials by allowing cyclic loading/unloading and reloading experiments using the shear device and enables the characterization of kinematic work hardening of sheet alloys. Many versions of simple shear devices have been used (Wack and Tourabi, 1993; Rauch, 1998; Lopes et al., 2003; Bouvier et al., 2006a,b; Fjeldly et al., 1998; Thuillier and Manach, 2009) on Al alloys; only recently simple shear experiments have been performed on the AZ31 alloy (Lou et al., 2007) at room temperature. No experimental data on simple shear experiments tests at high temperature have yet been reported in the literature.

Microtexture studies have been performed on AZ31 alloy using the EBSD technique in order to understand tensile (Del Valle et al., 2005; Jiang et al., 2007; Liu and Wu, 2006; Proust et al., 2009) and compression (Jiang et al., 2008; Choi et al., 2007) deformation modes. In addition, macrotextures were obtained by Jiang et al. (2007), Yi et al. (2006), Lou et al. (2007) and Agnew and Duygulu (2005) using X-ray diffraction and Jain et al. (2008), Brown et al. (2005), Muránsky et al. (2009) and Choi et al. (2007); using neutron diffraction, for (0 0 0 2) and $(1\,0\,\bar{1}\,0)$ pole figures. However, taken together, all the reported studies do not present a comprehensive set of experimental results from a single starting AZ31 sheet material on the stress–strain responses and texture evolution when deformed at different strain rates, temperatures and strain paths to enable calibration and validation of microstructure based plasticity models that are essential for fast development of materials and applications of Mg alloys. Twinning is known to be an athermal mode of deformation and known to play important role in high strain rate deformation (Mahajan and Williams, 1973; Christian and Mahajan, 1995). Jiang et al. (2007) have shown that the volume fraction of contraction and double twins increases with strain rate and decreases with temperature, becoming negligible above 200 °C in extruded AM30 and AZ31 tubes where grain sizes are over 10 μm. Tucker et al., 2009 have performed dynamic ($\sim$3800 s^{-1}) and quasi-static (10^{-3} s^{-1}) compression experiments on AZ31B-H24 and found strong strain rate dependency on the yield, hardening and failure strain in normal direction (ND) and almost none for in-plane directions. Ulacia et al. (2010) have shown similar observations for in-plane compression tests. However, for tension test in RD and TD there is significant variation in the yield strength with strain rate, where different deformation mechanisms are active. Maksoud et al. (2009) have performed quasi-static tensile experiments at room and elevated temperatures and found that the peak stresses decrease with decreasing strain rates, attributing this to the dynamic recrystallization process. What is not available in the literature is the data on the dependence of flow curve of Mg alloys on strain rate, temperature, texture and strain path for a common starting microstructure that can undergo deformation by slip and twinning.

The primary objective of this paper is to present a comprehensive set of results on a commercial grade AZ31 alloy under uniaxial (tension & compression) and multiaxial (simple shear) loading for a range of strain rates and temperatures. In addition to the mechanical response results, this study also includes detailed results on texture evolution under tensile and shear loading after finite deformation. The observed results are discussed briefly in light of known deformation mechanisms operating at different strain rates and temperatures under these strain paths. It is anticipated that these results, taken from a single batch of material, will assist the crystal plasticity models to be calibrated and validated. A strain rate and temperature dependent new constitutive model to accurately account for Mg deformation without grain boundary sliding will be developed in a subsequent publication on the basis of the data contained in this paper.

2. Experimental procedure

Experiments were performed on AZ31 sheet alloy (3wt%Al, 1wt%Zn, Mg bal.) which was tested in uniaxial tension, compression, and simple shear loading for quasi-static regime at room and elevated temperatures along rolling direction (RD), transverse to rolling direction (TD), and 45° to rolling direction (DD). Uniaxial compression experiments were also conducted with loading normal to the sheet plane (ND). The quasi-static experiments were carried out using a MTS tension/torsion servo-controlled loading frame at room temperature (25 °C) and elevated temperatures 65 °C and 150 °C; the strain rates were 10^{0} s^{-1}, 10^{-2} s^{-1}, and 10^{-4} s^{-1}. EBSD was used to document the initial texture of the sheet sample and after compression testing. Neutron diffraction was used to obtain the macrotexture of tensile specimens after failure and specimens deformed under simple shear loading. Fracture surfaces of some representative samples were examined in a scanning electron microscope after uniaxial tension tests.

2.1. Quasi-static uniaxial tension and compression experiments

Tension experiments for quasi-static loading were machined using ASTM-E8 and sub-sized dog-bone shaped specimens with a gage length of 31.0 mm (1.22 in.), gage width of 6.4 mm (0.252 in.), and 2.0 mm (0.0787 in.) thickness (sheet thickness). The in-plane anisotropy and the evolution of *r*-values with plastic strain at room temperatures were determined by mounting two high elongation strain gages (KFEL-2-120-C1) in the loading (ε_l^p) and transverse (ε_w^p) to loading directions. Quasi-static compression specimens in three (RD, TD, and DD) directions were prepared by bonding (using J-B Weld adhesive) two sheets with specimen dimensions of 12.7 mm (0.5 in.) length, 11.4 mm (0.45 in.) gage width, and 4.0 mm (0.157 in.) thickness. Pressure was applied and maintained after bonding the sheets together to remove the extra adhesive between the sheets. This enables to prepare specimen of uniform 4.04 mm (0.159 in.) thickness. Specimens were also prepared to perform experiments normal to the sheet direction (ND), and KFEL-2-120-C1 high elongation strain gages were used to measure the strains at room temperature. For high temperature compression experiments the stroke data was corrected using a blank test following the method of Khan et al. (2004).

2.2. Simple shear test

The simple shear specimen was prepared with a gage length of 38.2 mm (1.5 in.), a gage width of 6.0 mm (0.236 in.) and a thickness of 2.0 mm (0.0787 in) (sheet thickness) and specimens were sheared along the length using a simple shear device (Fig. 1). The shear device has two sections – (a) upper fixture, which holds the specimen using eight screws and (b) bottom

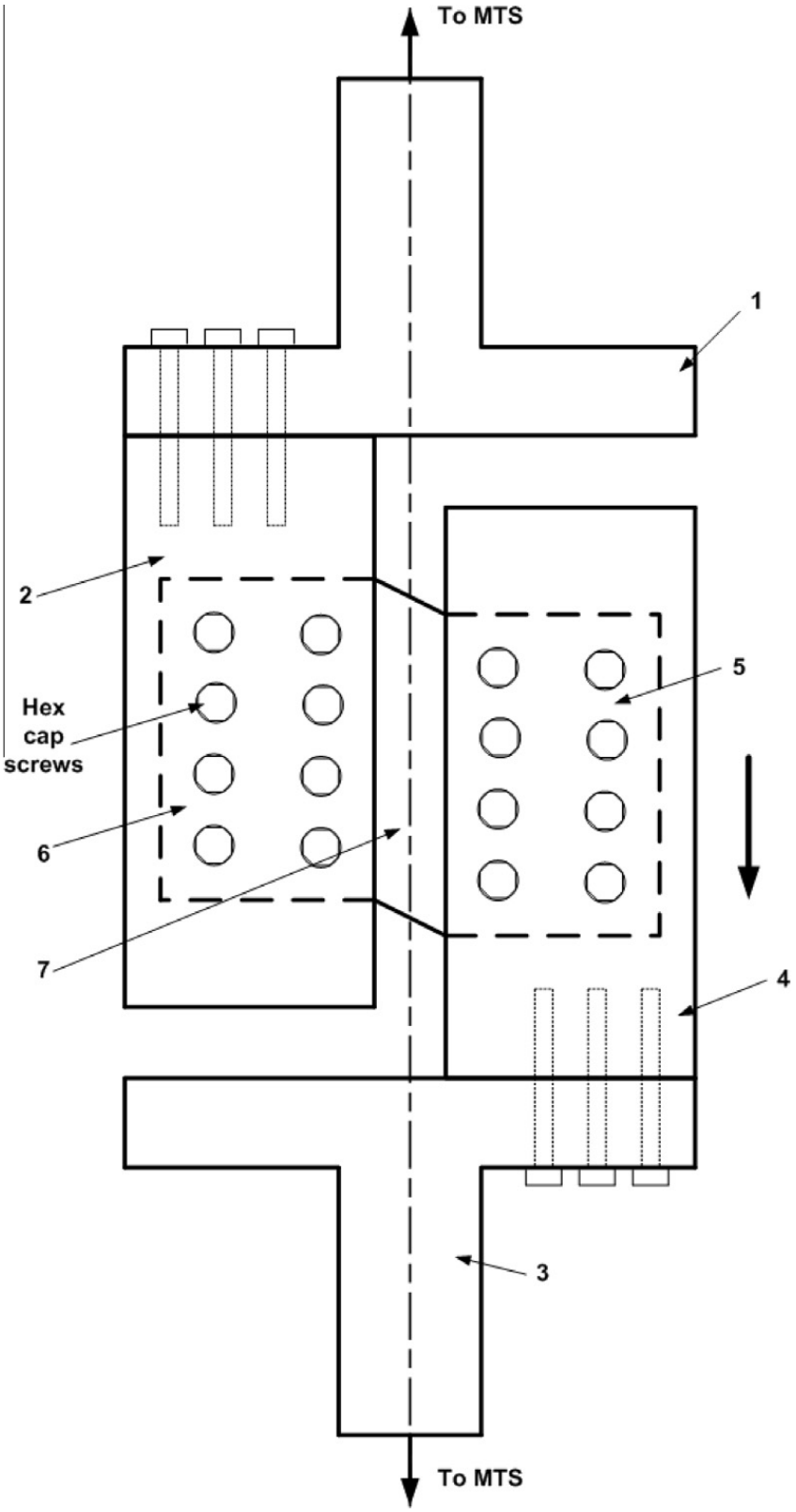

Fig. 1. Schematic section view of the simple shear fixture (1) upper fixture, (2) upper middle fixture, (3) bottom fixture, (4) bottom middle fixture, (5) movable grip section of shear specimen, (6) fixed grip section of shear specimen, and (7) gage section of shear specimen.

fixture, connected with the upper fixture with four screws. In this device, specimens were firmly gripped in the upper fixture using adjustable rigid blocks. For a given material, sample geometry and temperature, an optimum value of clamping force was applied to avoid sliding of specimens between the grips. Shear stress and shear strain were calculated from the load and vertical displacement, respectively, using the MTS tension/torsion system. Simple shear experiments were initially

performed on 50.8 mm (2 in.), 38.2 mm (1.5 in.), and 25.4 mm (1 in.) gage lengths with 6.0 mm gage width and the stress–strain responses for all lengths were found to be the same. A gage length of 38.2 mm was chosen for all shear experiments reported here.

2.3. Texture measurements

Neutron diffraction analysis was carried out on as-received sheet and deformed specimens using the BT8 residual stress diffractometer at the Center for Neutron Research, National Institute of Standards and Technology (NIST), Maryland, USA to measure textures of samples deformed under tension and simple shear at various directions, strain rates, and temperatures. Due to the instrument design with variable take-off angle (Brand et al., 1997), the wavelength was chosen to $\lambda = 0.223$ nm which made the AZ31 (magnesium) reflections $(10\bar{1}0)$, (0002), $(10\bar{1}1)$, $(11\bar{2}2)$ and $(20\bar{2}1)$ instrumentally accessible in the 2θ range from 46° to 116°. Three to four plates were cut from the uniformly deformed gage section using an Isomet wafering blade and a Buehler Isomet low speed saw. The plates were glued together to produce a near cube shaped specimen. Essentially all grains in the specimen volume (specimen gage section, about 0.2 cm^3) were illuminated by the neutron beam and contributed to diffracted intensity. The orientations in Euler space were chosen according to a scheme with 469 Euler angle orientations proposed by Matthies and Wenk (1992). The actual measurement consisted of varying the specimen orientation (with known specimen axis RD, TD, and ND) in Euler angles and successively measuring the diffracted intensity.

3. Results and discussion

3.1. Stress–strain responses

3.1.1. Yield stress and flow behavior

Figs. 2–4 show quasi-static tensile stress–strain responses in different directions at different strain rates and at different temperatures. All tensile specimens failed without any necking at room temperature in either the width or thickness directions, similar to the observations reported by Lou et al. (2007). The specimens at 65 °C necked before failure and necking was more predominant at 150 °C. The TD, DD and RD curves are highest, intermediate, and lowest strength at all strain rates and temperatures, respectively. In general, the yield and flow stresses decrease with temperature and the failure strain (total elongation) increases with temperature at all strain rates and all orientations. The n value at higher strain rate hardly changes with temperature from 25 °C to 150 °C but it drops by 60% for low strain rates in the same temperature range. The same trend is observed in RD, TD, and DD samples. The yield stresses for RD are lower than those for TD and DD (these being nearly identical) at all temperatures. Figs. 5–7 show quasi-static compressive stress–strain responses in different directions, strain rates, and temperatures. It is observed that the yield and flow stresses for in-plane tension and compression responses are largest for specimens oriented along TD and lowest for specimens oriented along RD for all strain rates and temperatures. The strength for specimens oriented along DD falls in between TD and RD similar to the results reported by Agnew and Duygulu, 2005. The yield stresses for in-plane compression are approximately half of the yield stresses in tension at room temperature and decrease at elevated temperatures at all strain rates. However, this decrease in yield stresses is much smaller at lower strain rates. The yield and failure strains at 10^0 s^{-1} strain rate (Fig. 5) are independent of temperature

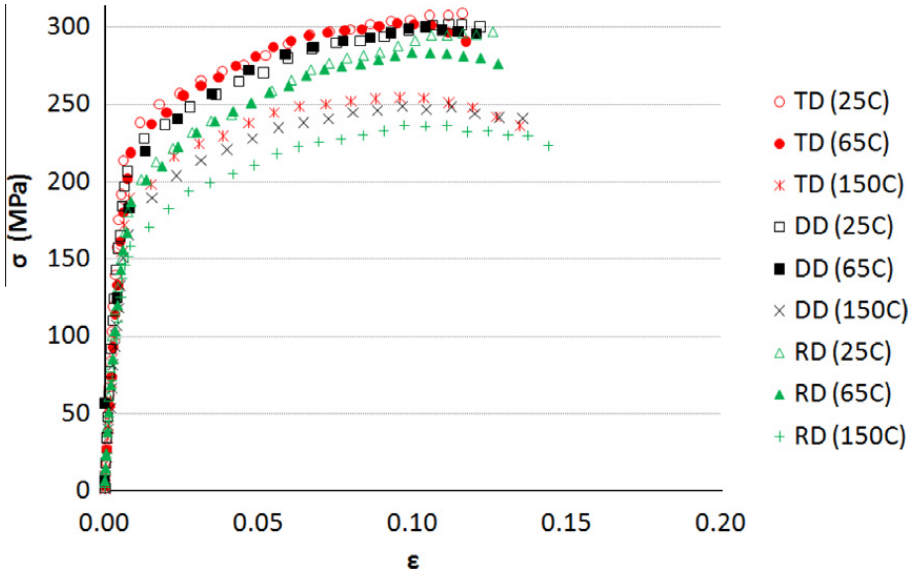

Fig. 2. Tension (true) responses at a strain rate of 10^0 s^{-1} at different temperatures and directions.

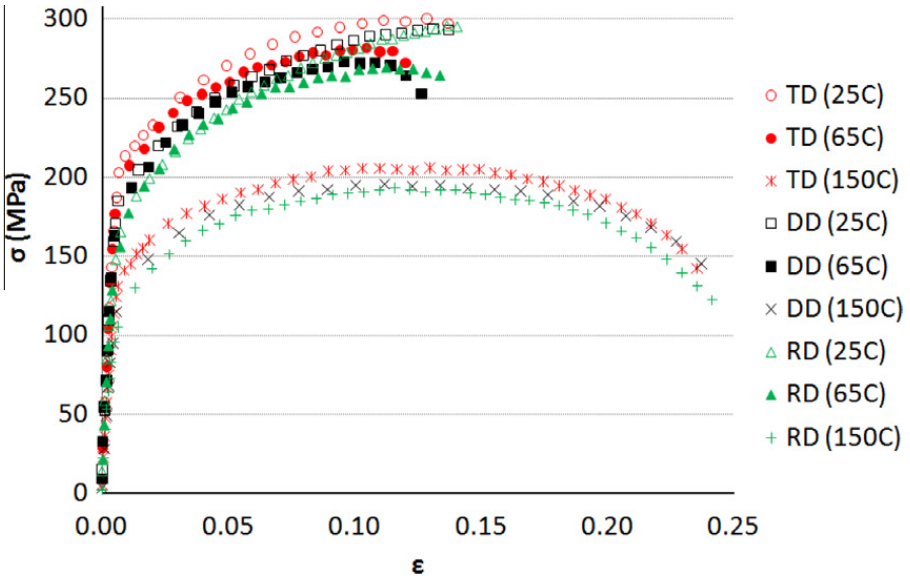

Fig. 3. Tension (true) responses at a strain rate of $10^{-2}\,s^{-1}$ at different temperatures and directions.

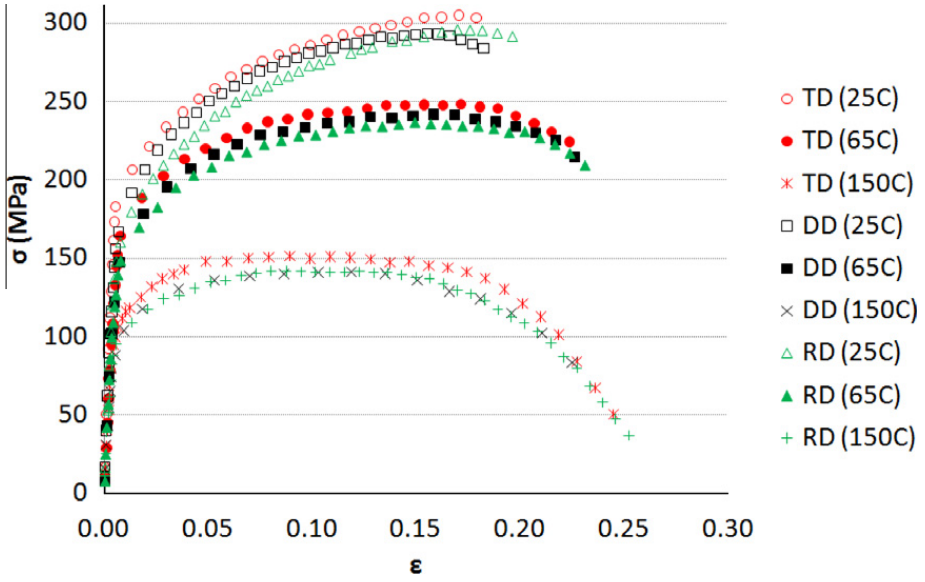

Fig. 4. Tension (true) responses at a strain rate of $10^{-4}\,s^{-1}$ at different temperatures and directions.

at 25 °C and 65 °C and the flow stresses are quite close. The in-plane compression stress–strain curves at 65 °C and 150 °C are initially close and deviate at higher strains, the inflection point in the compression curve being absent in the sample tested at the lowest strain rate for all orientations. The temperature effects are more pronounced in tension as compared to compression and at lower strain rates compared to higher strain rates. It is evident from Figs. 5–7 that the compressive yield and flow stresses strength is much higher in through thickness direction (ND) as compared to in-plane directions (RD, DD, and TD). Through thickness compression (ND) curve shows similar hardening characteristics as in-plane tension curves but has higher stress values for the same strain. The yield and flow stresses for through thickness compression (ND) as compared to in-plane compression or tension experiments are higher. The failure strains for ND specimens are smaller than the corresponding in-plane tension experiments. The compressive stress–strain curves in the sheet normal direction (ND) show strong dependence of yield and flow stresses on strain rate and temperature. Figs. 8–10 show simple shear curves at different strain rates, temperatures and direction. The yield and flow stresses observed from these curves shows similar trend as in the case of tension and compression with TD responses being the highest, RD lowest, and DD curves lie in between them. The response of the material to simple shear shows almost linear increase in flow stress with no sign of softening up to 20% equivalent shear strain and is thus completely different from those in tension (concave downward) and compression (concave upward) curves. The material exhibits positive strain rate sensitivity and the strain rate sensitivity increases with increase in temperatures.

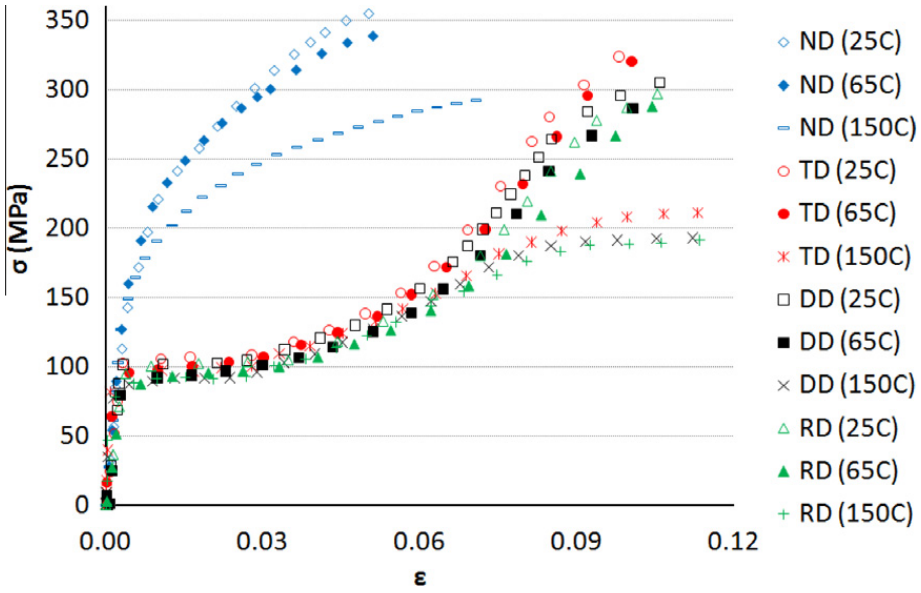

Fig. 5. Compression (true) responses at a strain rate of $10^0\ s^{-1}$ at different temperatures and directions.

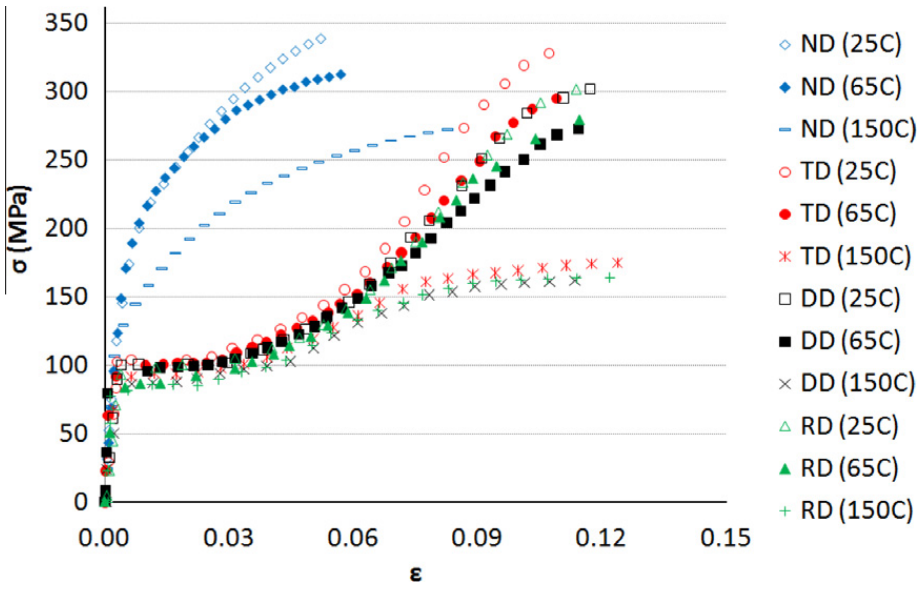

Fig. 6. Compression (true) responses at a strain rate of $10^{-2}\ s^{-1}$ at different temperatures and directions.

Higher ductility is generally associated with higher dislocation storage before fracture. This can occur if $\langle a \rangle$ dislocations are able to move from basal to prism and pyramidal-I planes, and interactions among these and non-basal $\langle c + a \rangle$ dislocations cause entanglement. The effect of increasing temperature is to have more slip systems activated, more mobility of dislocation, more cross slip and potential for higher dislocation entanglement and storage, leading to increased ductility. The results discussed above suggest that the effect of temperature on deformation may be quite significant without grain boundary sliding mechanisms which are known to be activated at higher temperatures. The variation of strength between specimens oriented along RD and TD, or DD is consistent with data presented in the literature, e.g. Agnew and Duygulu (2005), and is most likely due to the greater angular spread of basal poles towards RD than TD as will be discussed below from the texture data.

3.1.2. Strain rate sensitivity

The strain rate sensitivity m of the sheet along the RD, TD and DD at different temperatures for tension and compression are plotted for a strain value of 4% in Fig. 11. The material exhibit positive strain rate sensitivity at all test temperatures, strain rates, and directions in both compression and tension. The variation of m with temperature is small in compression but is non-zero and still positive. This is significant because the deformation modes at 4% strain in tension and compression are quite different, twinning dominating the deformation in in-plane compression as reflected in the s shaped stress–strain

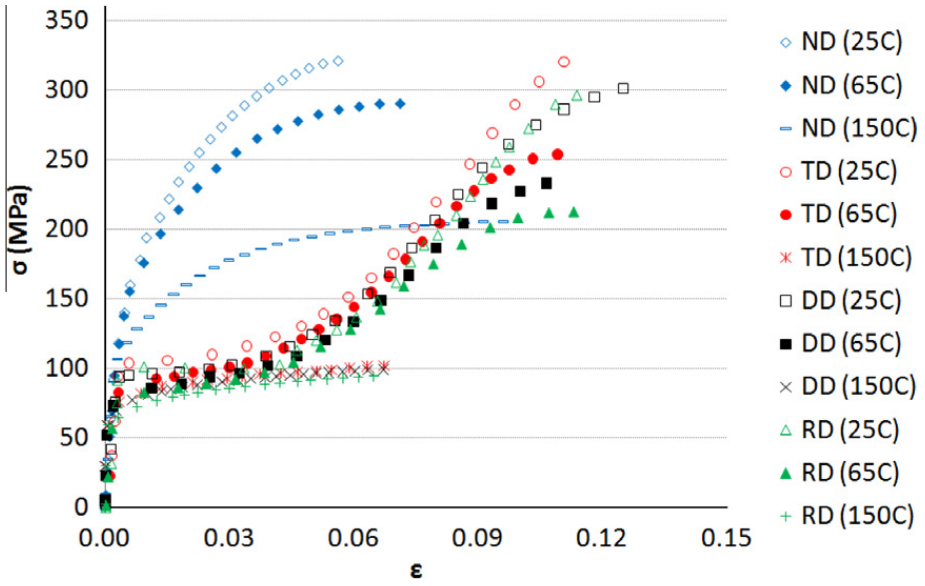

Fig. 7. Compression (true) responses at a strain rate of $10^{-4}\,s^{-1}$ at different temperatures and directions.

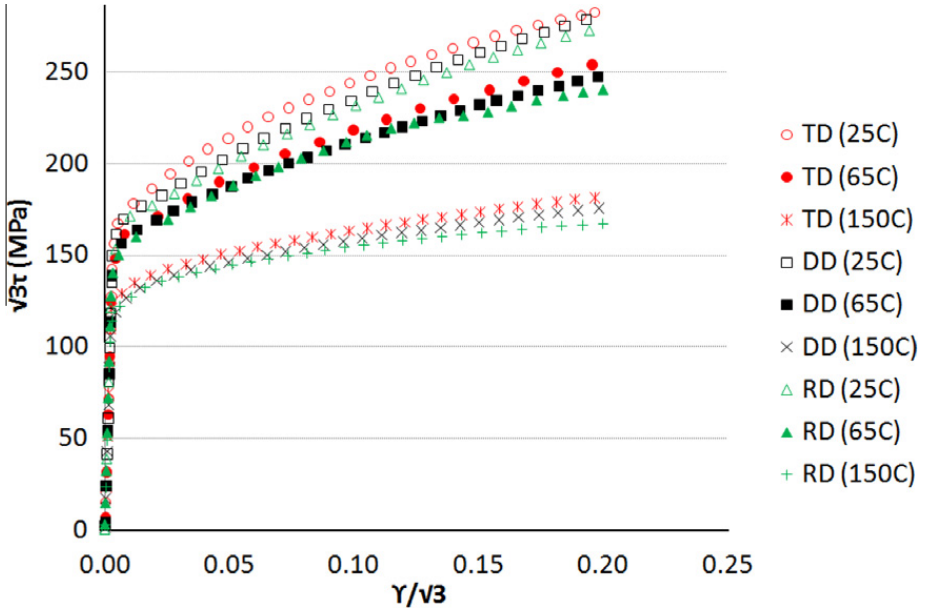

Fig. 8. Simple shear responses at a strain rate of $10^{0}\,s^{-1}$ at different temperatures and directions.

curve. The general shape and variation of tensile and compressive stress–strain curves are consistent with data already presented by various authors for AZ31 sheets. The classic sigmoid shape of the compression curves have been known to result from extension twinning which get exhausted at higher strain values, leading to large strain hardening (Jiang et al., 2007). At 150 °C and lower strain rate, the inflection point completely disappears in the in-plane compression sample. The shape of the stress–strain curves at room temperature and high strain rates, in particular the hardening behavior in tensile samples, ND compression samples and in-plane compression samples after the inflection point in the sigmoid curve when twinning is complete, are similar to the stress–strain curves in cubic metals in a general way, implying similar deformation mechanisms to be responsible for deformation. As will be discussed in the next section, the rate effect on twinning (manifested in the sigmoid shape of the flow curve) affects the texture.

3.1.3. Anisotropy of deformation

Fig. 12 shows the evolution of *r*-values (a measure of anisotropy of deformation) at room temperature with true axial strain at various strain rates and directions. Unlike the *r*-values for cubic materials, the *r*-value for AZ31 alloy increases with plastic deformation. The increase in *r*-value was greater in specimens oriented along TD and it is related to the transition

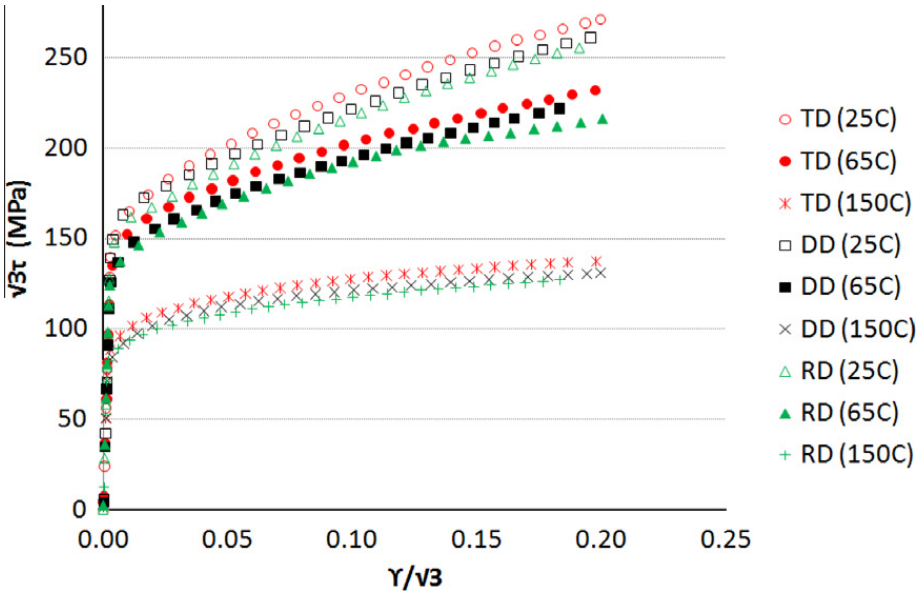

Fig. 9. Simple shear responses at a strain rate of $10^{-2}\,s^{-1}$ at different temperatures and directions.

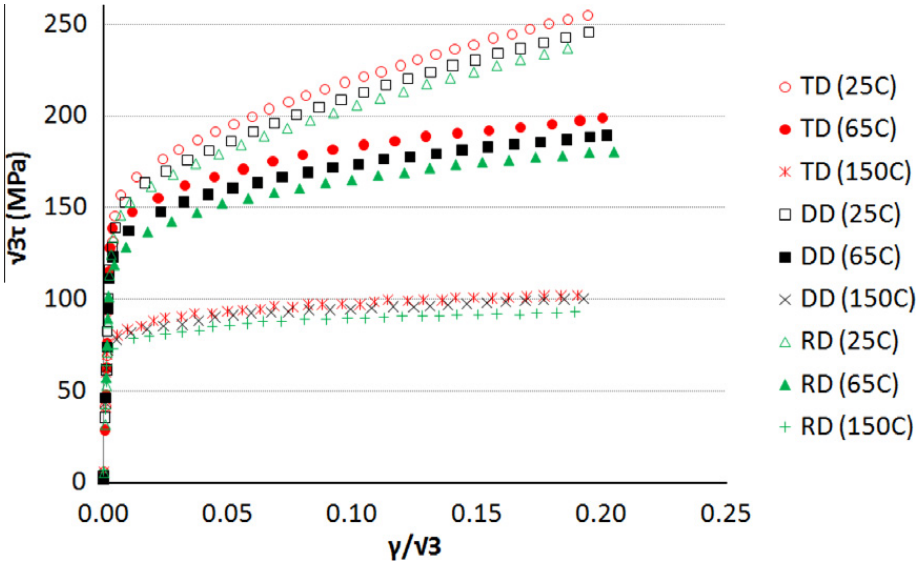

Fig. 10. Simple shear responses at a strain rate of $10^{-4}\,s^{-1}$ at different temperatures and directions.

from basal slip to non-basal slip (Lou et al., 2007). Also, the *r*-value increases with a decrease in strain rate for all three directions.

3.1.4. Rate of hardening

Figs. 13 and 14 show the variation of hardening rate with strain for tensile, compression and simple shear tests at 25 °C and 150 °C for $10^{0}\,s^{-1}$ and $10^{-4}\,s^{-1}$ strain rates. The hardening rate in compression tests at room temperature at both high and low strain rates first drops and then increases to a maximum before falling off again. The peak corresponds to about 9% strain where the stress–strain curve in Figs. 5 and 7 exhibit rapid hardening, corresponding to the end of twinning. This is confirmed by the texture data for a sample compressed to 8% strain using EBSD and will be discussed later. The sigmoid shape compression curve is present in all the compression data for higher strain rates but absent in the compression curve for lower strain rate at 150 °C. Detailed microstructural work is needed to determine if twinning is suppressed at 150 °C in this material, but previous studies of AZ31 extrusions by Jiang et al. (2007) suggests that twinning continues to occur beyond 200 °C. The absence of the sigmoid shape in the stress–strain curve in Fig. 7 and lack of the peak in the hardening curve in Fig. 14 suggest that twinning is no more the dominant mechanism for deformation in samples compressed at $10^{-4}\,s^{-1}$ strain rates at 150 °C where non-basal $\langle c+a\rangle$ dislocations must be quite active. The variation of hardening rates in tensile samples and simple shear samples show monotonic decrease with strain. The hardening values for the tensile samples at room

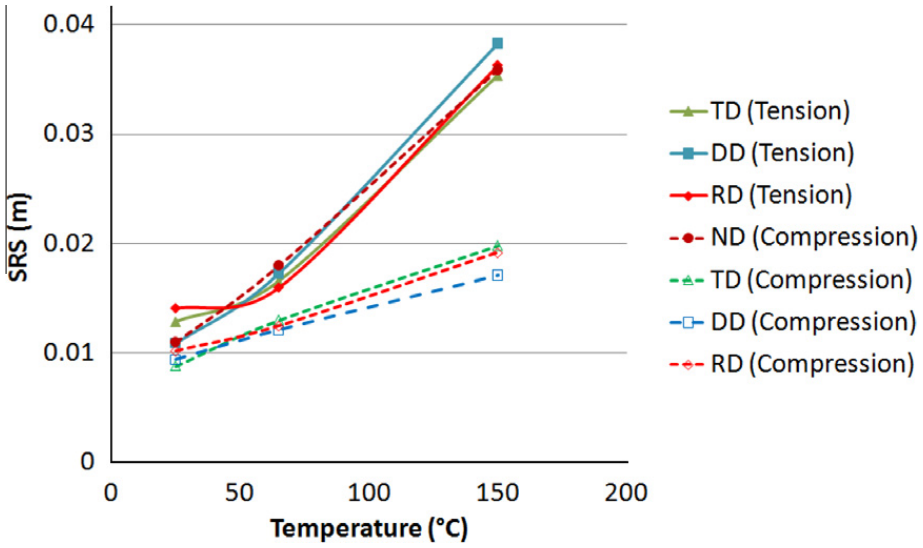

Fig. 11. Strain rate sensitivity at 4% strain under tension and compression at different temperatures and directions.

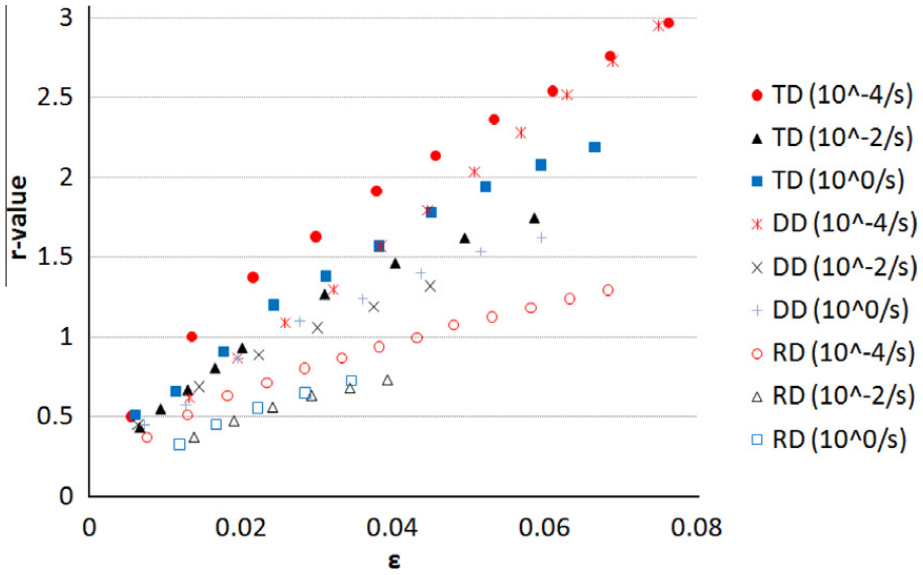

Fig. 12. Evolution of *r*-values at room temperatures (25 °C) for different strain rates and directions.

temperature is relatively high which could be related to contraction and double twinning (Jiang et al., 2007) and will require future microstructural characterization to ascertain. The different values of *n* at different temperatures and strain rates point to differences in the operative slip systems if one neglects the role of compression twins. These stress–strain curves are amenable for a power-law type fit for implementation in phenomenological formulation of sheet forming.

3.2. Texture evolution

3.2.1. Tension and compression

The EBSD inverse pole figure map (IPF) (Fig. 15) of the same as-received sheet material, confirm the above distribution of the grain orientations obtained by neutron diffraction. The grain size of the material is ~12 μm, above the size where twinning is normally observed. In addition, a small fraction of grains with their *c*-axis away from the sheet normal are observed. The large fractions of grains with the tilt (≈±10) towards +RD and −RD from the sheet normal are prone to twinning deformation. Fig. 16 shows the $(0\,0\,0\,1)$, and $(1\,0\,\bar{1}\,0)$, pole figure plots of the as-received AZ31 sheet in the recrystallized condition obtained using neutron diffraction. The macrotexture data shows that the *c*-axes in the grains are slightly tilted away from the sheet normal and lie on the ND–RD plane, thereby giving rise to an ellipsoidal intensity distribution in the $(0\,0\,0\,1)$ pole figure. The intensity distribution in the pole figures for prismatic $(1\,0\,\bar{1}\,0)$ planes show diffuse intensity maxima at the north and south poles of the stereographic projection and the pole figures for the pyramidal-I $(1\,0\,\bar{1}\,1)$ and pyramidal-II $(1\,1\,\bar{2}\,2)$

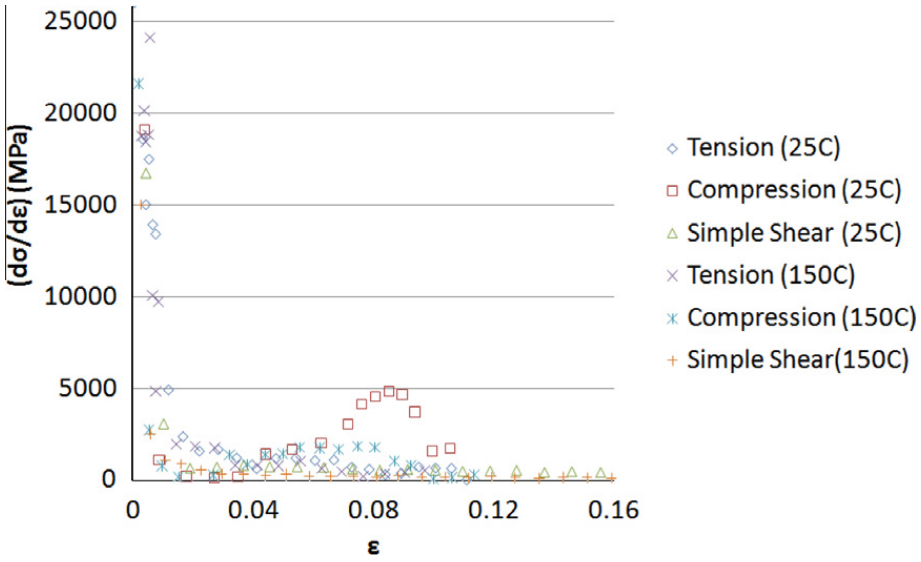

Fig. 13. Rate of hardening rate with strain for tensile, compression, and simple shear tests at $10^0\ s^{-1}$ strain rate at different temperatures and in RD.

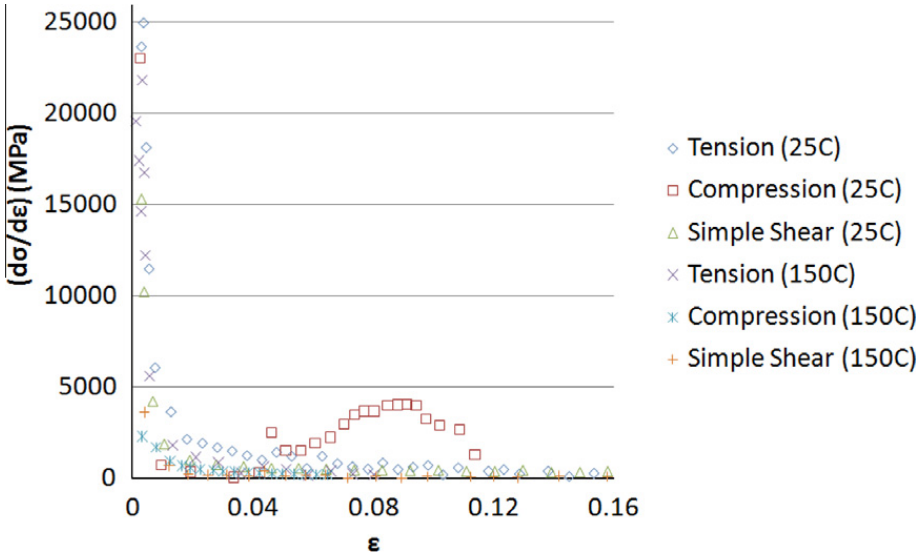

Fig. 14. Rate of hardening rate with strain for tensile, compression, and simple shear tests at $10^{-4}\ s^{-1}$ strain rate at different temperatures in RD.

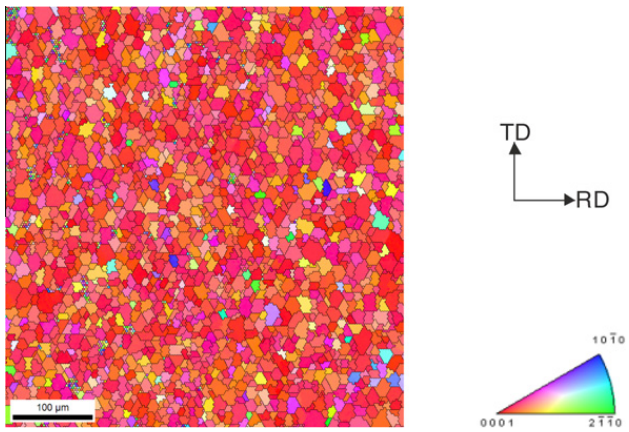

Fig. 15. Inverse pole figure (IPF) EBSD map of as-received sheet.

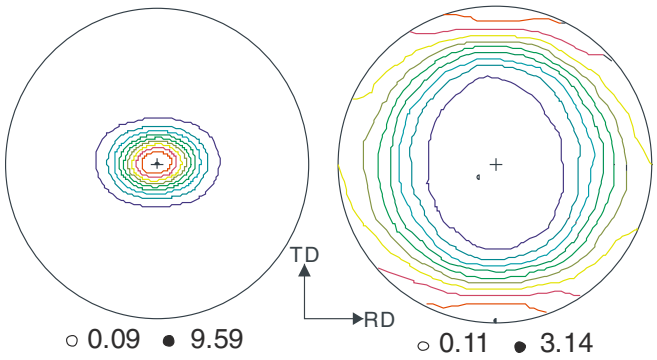

Fig. 16. (0 0 0 2) (left) and (1 0 $\bar{1}$ 0) (right) pole figures of as-received sheet.

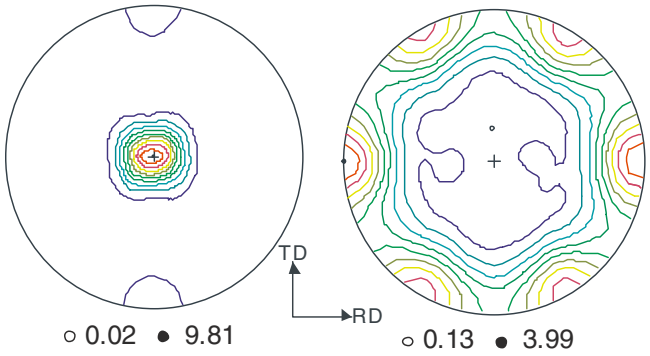

Fig. 17. (0 0 0 2) (left) and (1 0 $\bar{1}$ 0) (right) pole figures after tensile failure in RD at room temperature (25 °C) and strain rate of 10^0 s^{-1}.

planes show diffuse intensity maxima along the polar direction at appropriate angles away from the *c*-axis. Only the basal and the prismatic pole figures are shown in the remainder of the paper for the deformed samples for clarity but the pyramidal pole figures can be easily visualized with their intensity maxima at appropriate angles from the basal and prism poles. The data suggests that the crystallites are oriented such that their *c*-axes are nearly normal to the sheet plane with a tilt along the RD, the prism planes show a dominant orientation parallel to the RD (and normal to TD). Other orientations of the prism planes appear weak. Figs. 17 and 18 show the pole figures from samples that have been deformed to tensile failure at 10^0 s^{-1} and 10^{-4} s^{-1} strain rates at room temperature. The data from samples deformed at strain rate of 10^{-2} s^{-1} fall in between the data for samples deformed at these two strain rates and are not included here for brevity. Fig. 19 shows the basal and prismatic plane pole figures from a specimen deformed to 4% tensile strain at 10^0 s^{-1} strain rate at room temperature. It is clear from Figs. 17–19 that as the sheet deforms at room temperature along the RD at either strain rate, the basal planes rotate to lie parallel to the sheet surface and the tensile axis. This must be the result of basal dislocation activity in favorably oriented grains. In the simple model of lattice rotation during tensile deformation, the slip planes tend to rotate to lie parallel to the tensile axis and this suggests that basal slip dominated the deformation at low strains at room temperature. The effect of lattice rotation is most pronounced on the changes in the intensity distribution of the prismatic planes. The intensity maxima in the (1 0 $\bar{1}$ 0) pole figures are now well developed, appearing in the hexagonal positions separated by 60° from each other along the perimeter of the stereographic projection with no intensity maxima at the poles in Figs. 17 and 18. The intensity distribution corresponding to the prism planes is even pronounced in Fig. 19, after the sample has been deformed to a small strain level of just 4%. None of the prism planes are parallel to the tensile axis. The intensity distribution at the poles in the (0 0 0 2) pole figures in Figs. 17 and 18 suggest that some twinning has occurred at large deformations to rotate the lattice by 86° degrees (tensile twin on (1 0 $\bar{1}$ 2) planes). There is no intensity corresponding to such twinning in Fig. 20 at 4% strain. The amount of material twinned at high strains must be very small as the intensity value corresponding to twinning reflections is close to 1 while basal pole intensity corresponds to a value of 10 in Figs. 17 and 18. Figs. 20 and 21 show the pole figures after tensile failure at strain rates of $10^0 s^{-1}$ and 10^{-4} s^{-1} at 150°C. The change in the orientation of the grains is similar to what occurs at room temperature except that no intensity corresponding to twinning is present at the higher temperature. The basal and the prismatic plane texture are well developed. In Figs. 17–21, the intensity maxima values in (0 0 0 2) pole figures are slightly higher for sample deformed at the lower strain rate. In addition to the above tests, one specimen was compressed in RD to 8% strain at room temperature at 10^0 s^{-1} strain rate and was examined by EBSD. The texture plot (Fig. 22) as well as the IPF map (Fig. 23) shows that the *c*-axes of the grains lie nearly parallel to the loading direction (RD). Extension twinning in Mg rotates the basal plane by 86° and this must have been the dominant mode of deformation, similar to those reported by others. The prismatic planes now lie at an angle to the sheet surface as shown

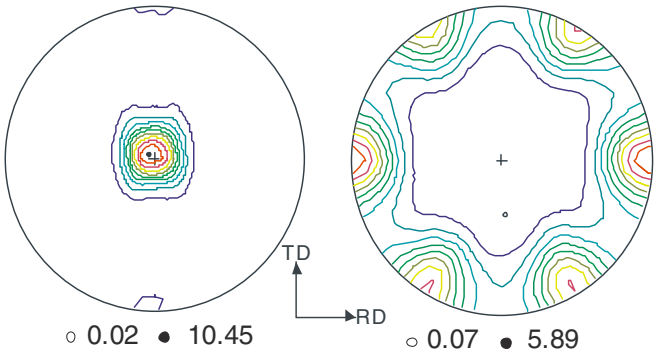

Fig. 18. (0 0 0 2) (left) and (1 0 $\bar{1}$ 0) (right) pole figures after tensile failure in RD at room temperature (25 °C) and at the strain rate of 10^{-4} s^{-1}.

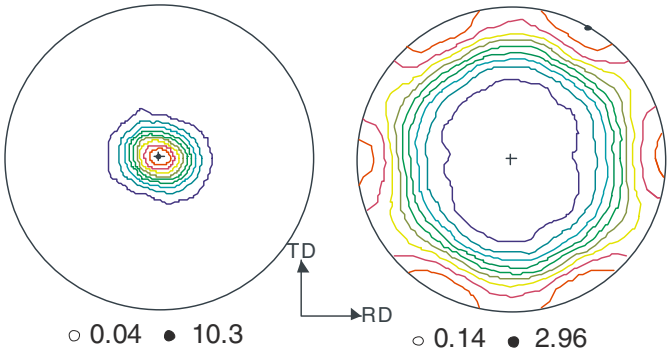

Fig. 19. (0 0 0 2) (left) and (1 0 $\bar{1}$ 0) (right) pole figures after tensile failure in RD after 4% tensile deformation at room temperature (25 °C) and at the strain rate of 100 s^{-1}.

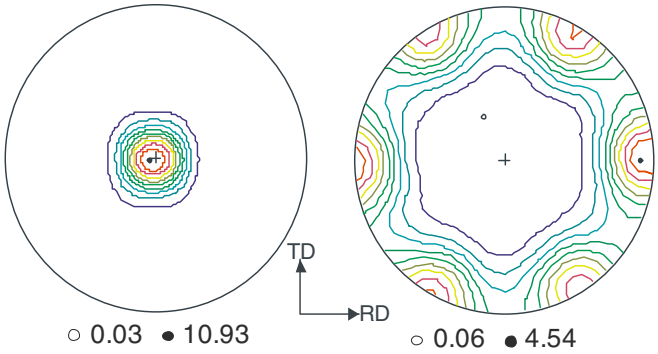

Fig. 20. (0 0 0 2) (left) and (1 0 $\bar{1}$ 0) (right) pole figures after tensile failure in RD at 150 °C in RD at the strain rate of 10^{0} s^{-1}.

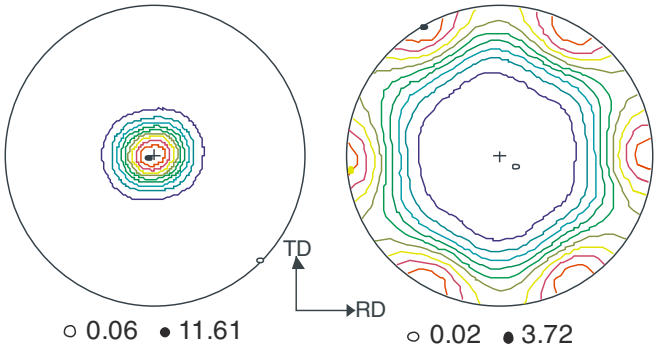

Fig. 21. (0 0 0 2) (left) and (1 0 $\bar{1}$ 0) (right) pole figures after tensile failure in RD at 150 °C in RD at the strain rate of 10^{-4} s^{-1}.

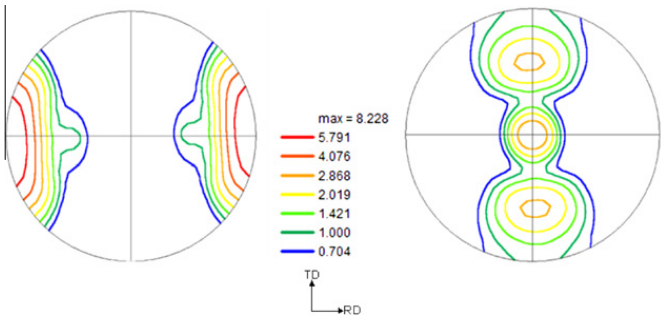

Fig. 22. (0 0 0 2) (left), and (1 0 $\bar{1}$ 0) (right) pole figures after 8% deformation under compression loading in RD at room temperature (25 °C) and strain rate of 10^0 s^{-1} (texture from EBSD data)

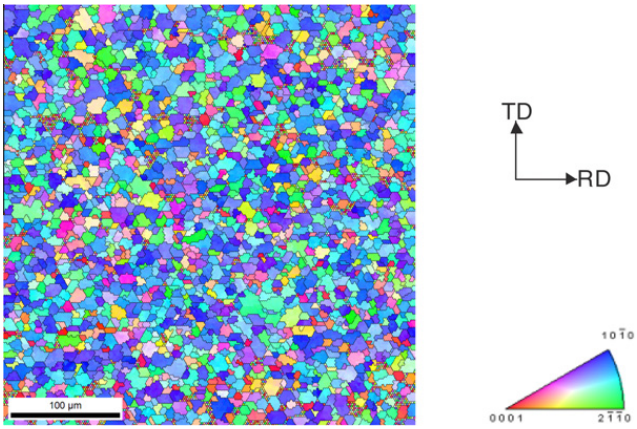

Fig. 23. Inverse pole figure (IPF) EBSD map after 8% deformation under compression loading in RD at room temperature (25 °C) and strain rate of 10^0 s^{-1}.

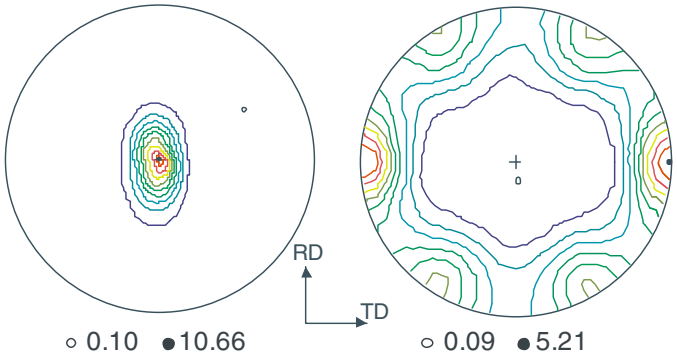

Fig. 24. (0 0 0 2) (left) and (1 0 $\bar{1}$ 0) (right) pole figures after tensile failure in TD at 150 °C and strain rate of 10^{-4} s^{-1}.

by the (1 0 $\bar{1}$ 0) texture plot. A semi-quantitative area fraction measurement of the twinned grains shows over 80% of the grains to be in the twinned orientation. Unlike tension along RD (Figs. 17–19) which align the *c*-axes of the grains normal to the sheet plane, loading along TD does not reorient the *c*-axes of the hexagonal lattice from their original tilted positions along the RD. The texture data in Fig. 24, taken from a sample deformed at 150 °C where many slip systems can be active, shows that the (0 0 0 2) peak is still elliptical and the (1 0 $\bar{1}$ 0) peak is still predominantly along the TD. The main difference between the texture of the deformed and the undeformed sample is in the appearance of intensities at 60° intervals on the perimeter of the (1 0 $\bar{1}$ 0) pole figure. Such texture data is consistent with minimal dislocation activity on the basal or prismatic planes which do not rotate towards the tensile axis. The tensile data in Figs. 2 and 3 shows the TD samples to have highest flow stresses at all temperatures and strain rates. The higher strength and hardening of the TD specimens compared to RD specimens, especially at lower temperatures, must result from a lack of easy dislocation glide.

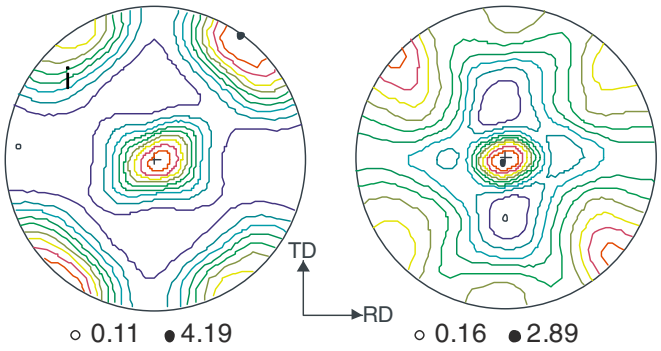

Fig. 25. (0 0 0 2) (left) and (1 0 $\bar{1}$ 0) (right) pole figures after simple shear loading in RD at room temperature (25 °C) and strain rate of 10^0 s^{-1}.

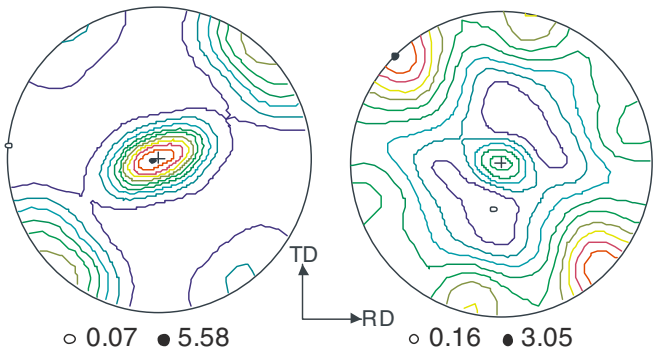

Fig. 26. (0 0 0 2) (left) and (1 0 $\bar{1}$ 0) (right) pole figures after simple shear loading in RD at room temperature (25 °C) and strain rate of 10^{-4} s^{-1}.

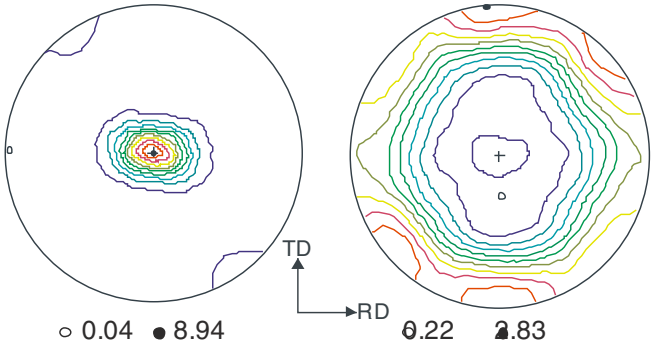

Fig. 27. (0 0 0 2) (left) and (1 0 $\bar{1}$ 0) (right) pole figures after simple shear loading in RD at 150 °C and strain rate of 10^0 s^{-1}.

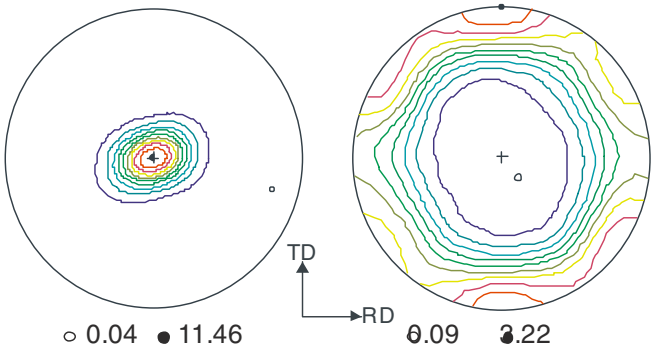

Fig. 28. (0 0 0 2) (left) and (1 0 $\bar{1}$ 0) (right) pole figures after simple shear loading in RD at 150 °C at the strain rate of 10^{-4} s^{-1}.

3.2.2. Simple shear

The texture data after simple shear loading, shown in Figs. 25–30 show intensity distributions that may be considered as a complex combination of the tensile and the compression sample texture data discussed above. The basal pole intensity is elongated 45° away from the shear direction. In addition, intensity maxima corresponding to ~90° rotation of the *c*-axis to lie on the sheet plane along two mutually orthogonal directions at 45° away from the RD appear in the pole figure for samples deformed at room temperature. The intensities corresponding to the in-plane *c*-axes in these samples sheared at higher strain rate are stronger than those deformed at lower strain rate. In the sample deformed at 150°C, intensities corresponding to in-plane *c*-axes disappear at low strain rate and appear very weak at higher strain rate. The texture data is consistent with the sample undergoing extension twinning to reorient the *c*-axis by ~86° under in-plane compressive loading in mutually orthogonal directions on the sheet surface oriented 45° from the shear direction. To achieve simple shear, the sample was subjected to an external compressive load normal to the shear direction. The components of the strain path experienced by the sample were a combined compressive and tensile loading at 45° to RD and compressive loading normal to this

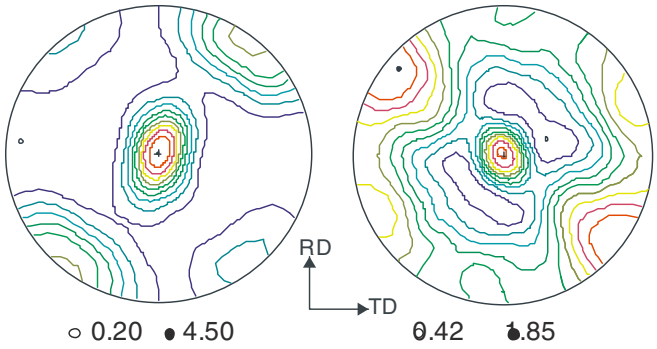

Fig. 29. (0 0 0 2) (left) and (1 0 $\bar{1}$ 0) (right) pole figures after simple shear loading in TD at room temperature (25 °C) and strain rate of $10^0\ s^{-1}$.

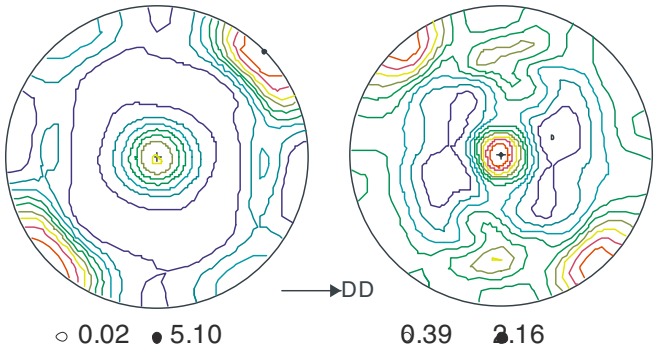

Fig. 30. (0 0 0 2) (left) and (1 0 $\bar{1}$ 0) (right) pole figures after simple shear loading in D.D. at room temperature (25 °C) and strain rate of $10^0\ s^{-1}$.

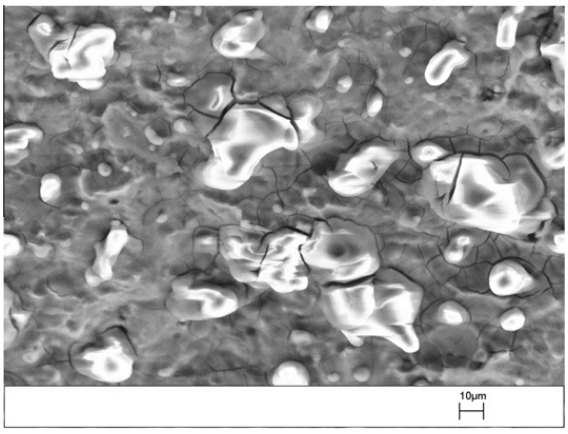

Fig. 31. Fracture surface of the tensile specimen deformed in RD at the strain rate of $10^{-2}\ s^{-1}$ at room temperature (25 °C).

direction. The texture data in the (0 0 0 2) projections from samples deformed in simple shear at RT at strain rate of 10^0 s^{-1} (Figs. 31 and 32) shows that the elliptical distribution of the intensity corresponding to the basal planes in the as-received sample remains unchanged in TD specimens but becomes circular in the DD specimens as if the sample was deformed in tension along an axis 45° away from the DD.

The relative fraction of this intensity with respect to the total intensity of the respective (0 0 0 2) pole figure is shown in Table 1. The twin volume fraction can be determined in an analysis similar to Jiang et al., (2007) through assigning the intensity (with weight $\sin\psi$) in the interval $\psi = (75°, 90°)$ and $\varphi = (0°, 360°)$ to deformation twinning. The rationale of the determination of the volume fraction of deformation twins is that for moderate elongations of 10–20% only twinning can cause substantial grain rotations. Thus, the appearance of intensity in the periphery of (0 0 0 2) pole figures can be attributed to '86' deformation twins. This approach was chosen because of the straight-forward relationship between twin orientation and intensity. In more complex cases this analysis is done in orientation space, i.e. through the calculation of the orientation distribution function (ODF) in which the frequency of twin associated grain orientations (relative to the integral over the entire ODF) is determined. The few observations evident from Table 1 are (a) simple shear specimens have high volume fraction of twin deformation as compared to the tension specimens. Since, one of the orthogonal axes during simple shear deformation undergoes compression and involves extension twinning during deformation. (b) There is an increase in twin intensity with increase in strain rate, and (c) the volume fraction of twin intensity decreases with increase in test temperature as more slip (including non-basal) planes are available for dislocation glide.

3.2.3. Fracture surface

Figs. 31 and 32 compares the fracture surfaces of the RD tensile specimen deformed at 10^{-2} s^{-1} at room temperature and at 150 °C. The SEM image clearly indicates a dimpled ductile fracture surface for the sample deformed at 150 °C. However, a quasi-brittle intergranular fracture surface is observed in the sample fractured at room temperature. The EBSD map in Fig. 15 shows many grains in the sheet material that do not have their *c*-axes parallel to the sheet normal and those would exhibit very different deformation behavior compared to the other grains. Lacking easy activation of basal and non-basal dislocations and twins to accommodate general deformation at room temperature in any grain, and with negligible grain boundary sliding activity at room temperature, grains adjacent to these grains will not able to deform simultaneously to maintain the integrity of the material, leading to decohesion and cracking at the grain boundaries. At 150 °C, where more slip systems are activated, the inhomogeneous deformation in adjacent grains is accommodated by slip mechanisms (and even some grain boundary sliding). The appearance of the dimpled fracture surface at 150 °C is consistent with intragranular failure due to void formation and coalescence from dislocation activity.

The stress–strain figures suggests that the yield strength for shear is in between that for tension and compression at all strain rates and temperatures and the drop in Y.S. with temperature for simple shear is less than that for tension but more than that in compression. The origin of intensity differences on the perimeter in Figs. 25 and 26 that would correspond to different amount of twinning at high and low strain rates at room temperature is unclear. The stress–strain curves in simple shear also do not contain any evidence of the characteristic S-shape and a complete understanding of the relationship between the stress–strain curves and texture requires further experimental studies and modeling. The texture data in Figs. 27 and 28 show nearly no change in texture during simple shear at 150 °C, especially at low strain rate. This will be consistent with grain boundary sliding but requires detailed micro-structural studies to verify. The work hardening rates for simple shear do not exhibit the high work hardening rates associated with twinning at room temperature and fall off rapidly to a nearly zero value, characteristic of steady state dynamic evolution of the microstructure. Future analysis of the data presented here can develop the constitutive laws that best describe the deformation behavior while taking into account the associated micro-structural changes and the mechanisms of deformation.

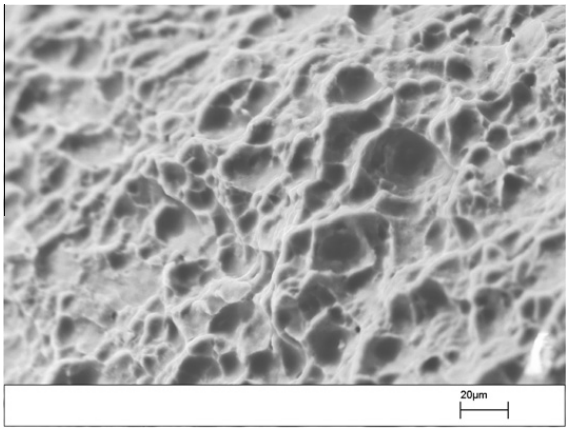

Fig. 32. Fracture surface of the tensile specimen deformed in RD at the strain rate of 10^{-2} s^{-1} at 150 °C.

Table 1
Volume fraction of extension twins in tension and shear samples. The values are normalized (i.e. 0.028 was subtracted) to the as-received sample.

Loading direction	S.R. (s^{-1})	Temp. (°C)	Vol. fraction of deformation twins
Tension (RD)	10^{-4}	150	0
Tension (TD)	10^{-4}	150	0
Simple shear (RD)	10^{-4}	150	0.002
Simple shear (TD)	10^{-4}	150	0.01
RD (4%)	10^{0}	25	0.021
Tension (DD)	10^{-4}	65	0.024
Tension (RD)	10^{0}	150	0.031
Simple shear (DD)	10^{-2}	150	0.045
Tension (RD)	10^{-4}	25	0.056
Tension (DD)	10^{0}	25	0.065
Tension (RD)	10^{0}	25	0.076
Simple shear (RD)	10^{0}	150	0.135
Simple shear (DD)	10^{-4}	65	0.17
Simple shear (TD)	10^{-2}	65	0.304
Simple shear (RD)	10^{-4}	25	0.381
Simple shear (DD)	10^{-2}	65	0.383
Simple shear (TD)	10^{0}	25	0.408
Simple shear (RD)	10^{0}	25	0.506
Simple shear (DD)	10^{0}	25	0.548

4. Conclusions

The results presented in this study include comprehensive stress–strain responses and pole figures for one AZ31 sheet alloy at different strain rates, temperatures, and loading paths. The material showed positive SRS at room temperature and the SRS increased with increase in temperatures. The yield and flow stresses for ND compression curves followed similar characteristics as in-plane tension at all strain rates and temperatures. The temperature sensitivity of the material increased with decrease in the strain rate. The failure strains were larger at low strain rates and higher temperatures. The sheet alloy had higher strength in TD. It was observed that when the specimen was deformed at room temperature along the RD, the grains align to produce a sharp texture. Also, a small amount of twinning occurred at high strains to rotate the lattice by 86°. However, at higher temperatures, the change in the orientation of the grains was similar to the room temperatures but no twinning was observed after large deformation. The fracture surface clearly indicated a fully ductile fracture at elevated temperatures and quasi-brittle fracture at the room temperature. The pole figures obtained after compression loading showed extension twinning rotating the *c*-axes to lie parallel to the loading direction. However, loading along the TD did not alter the elliptical shape of the (0 0 0 2) peak in the pole figure. Finally, pole figures after simple shear loading showed the material to be prone to extension twinning which rotated the *c*-axis from being normal to the sheet to lie parallel to the "compression" axis. However at higher temperatures twins were suppressed and was most probably non-basal deformation was accommodated by $\langle c + a \rangle$ Slip. The data presented here is a complete representation of mechanical response and accompanying microstructure evolution during deformation under a variety of strain paths at different temperatures and strain rates in AZ31 sheets and can be of immense value for calibration and validation of crystal plasticity and phenomenological models.

Acknowledgement and Disclaimer

The authors wish to thank Dr. Vladimir Luzin, ANSTO (Australia) for his software program QPFV used to produce the mesh and graphical pole figures. Certain commercial firms and trade names are identified in this report in order to specify aspects of the experimental procedure adequately. Such identification is not intended to imply recommendation or endorsement by the National Institute of Standards and Technology, nor is it intended to imply that the materials or equipment identified are necessarily the best available for the purpose.

The authors are appreciative of GM Corp. for providing the material for this study.

References

Abu-Farha, F.K., Khraisheh, M.K., 2007. Mechanical characteristics of superplastic deformation of AZ31 magnesium alloy. J. Mater. Eng. Perform. 16, 192–199.

Aghion, E., Bronfin, B., Eliezer, D., 2001. The role of the magnesium industry in protecting the environment. J. Mater. Process. Technol. 117, 381–385.

Agnew, S.R., Duygulu, Ö., 2005. Plastic anisotropy and the role of non-basal slip in magnesium alloy AZ31B. Int. J. Plasticity 21, 1161–1193.

Agnew, S.R., Yoo, M.H., Tome, C.N., 2001. Application of texture simulation to understanding mechanical behavior of Mg and solid solution alloys containing Li or Y. Acta Mater. 49, 4277–4289.

Agnew, S.R., Tomé, C.N., Brown, D.W., Holden, T.M., Vogel, S.C., 2003. Study of slip mechanisms in a magnesium alloy by neutron diffraction and modeling. Scripta Mater. 48, 1003–1008.

Al-Samman, T., Gottstein, G., 2008. Dynamic recrystallization during high temperature deformation of magnesium. Mater. Sci. Eng. A 490, 411–420.

Backofen, W.A., Avery, D.H., Turner, J.R., 1964. Superplasticity in Al–Zn Alloy. Trans. Am. Soc. Metals, 980–990.

Boger, R.K., Wagoner, R.H., Barlat, F., Lee, M.G., Chung, K., 2005. Continuous, large strain, tension/compression testing of sheet material. Int. J. Plasticity 21, 2319–2343.
Bouvier, S., Gardey, B., Haddadi, H., Teodosiu, C., 2006a. Characterization of the strain-induced plastic anisotropy of rolled sheets by using sequences of simple shear and uniaxial tensile tests. J. Mater. Process. Technol. 174, 115–126.
Bouvier, S., Haddadi, H., Levée, P., Teodosiu, C., 2006b. Simple shear tests: experimental techniques and characterization of the plastic anisotropy of rolled sheets at large strains. J. Mater. Process. Technol. 172, 96–103.
Brand, P.C., Prask, H.J., Herold, T.G-., 1997. Residual stress measurements at the NIST reactor. Phys. B: Condens. Matter 241–243, 1244–1245.
Brown, D.W., Agnew, S.R., Bourke, M.A.M., Holden, T.M., Vogel, S.C., Tomé, C.N., 2005. Internal strain and texture evolution during deformation twinning in magnesium. Mater. Sci. Eng. A 399, 1–12.
Chino, Y., Kimura, K., Mabuchi, M., 2008. Twinning behavior and deformation mechanisms of extruded AZ31 Mg alloy. Mater. Sci. Eng. A 486, 481–488.
Choi, H.S-., Shin, E.J., Seong, B.S., 2007. Simulation of deformation twins and deformation texture in an AZ31 Mg alloy under uniaxial compression. Acta Mater. 55, 4181–4192.
Christian, J.W., Mahajan, S., 1995. Deformation twinning. Prog. Mater. Sci. 39, 1–157.
Del Valle, J.A., Pérez-Prado, M.T., Ruano, O.A., 2005. Deformation mechanisms responsible for the high ductility in a Mg AZ31 alloy analyzed by electron backscattered diffraction. Metall. Mater. Trans. A 36, 1427–1438.
Fjeldly, A., Roven, H.J., Rauch, E., 1998. Shear deformation properties of extruded AlZnMg alloys. Scripta Mater. 38, 709–714.
Helis, L., Okayasu, K., Fukutomi, H., 2006. Microstructure evolution and texture development during high-temperature uniaxial compression of magnesium alloy AZ31. Mater. Sci. Eng. A 430, 98–103.
Hilditch, T., Atwell, D., Easton, M., Barnett, M., 2009. Performance of wrought aluminium and magnesium alloy tubes in three-point bending. Mater. Design 30, 2316–2322.
Jain, A., Agnew, S.R., 2007. Modeling the temperature dependent effect of twinning on the behavior of magnesium alloy AZ31B sheet. Mater. Sci. Eng. A 462, 29–36.
Jain, A., Duygulu, O., Brown, D.W., Tomé, C.N., Agnew, S.R., 2008. Grain size effects on the tensile properties and deformation mechanisms of a magnesium alloy AZ31B sheet. Mater. Sci. Eng. A 486, 545–555.
Jiang, L., Jonas, J., Mishra, R., Luo, A., Sachdev, A., Godet, S., 2007. Twinning and texture development in two Mg alloys subjected to loading along three different strain paths. Acta Mater. 55, 3899–3910.
Jiang, J., Godfrey, A., Liu, W., Liu, Q., 2008. Microtexture evolution via deformation twinning and slip during compression of magnesium alloy AZ31. Mater. Sci. Eng. A 483–484, 576–579.
Khan, A.S., Kazmi, R., Pandey, A., Stoughton, T., 2009. Evolution of subsequent yield surfaces and elastic constants with finite plastic deformation. Part I: a very low work hardening aluminum alloy: Al-6061–T 6511. Int. J. Plasticity 25, 1611–1625.
Khan, A.S., Pandey, A., Stoughton, T., 2010a. Evolution of subsequent yield surfaces and elastic constants with finite plastic deformation. Part II: a very high work hardening aluminum alloy (annealed 1100 Al). Int. J. Plasticity 26, 1421–1431.
Khan, A.S., Pandey, A., Stoughton, T., 2010b. Evolution of subsequent yield surfaces and elastic constants with finite plastic deformation, part-III: Yield surface in tension- tension stress space (Al 6061-T 6511 & annealed 1100 Al). Int. J. Plasticity 26, 1432–1441.
Khan, A.S., Suh, Y.S., Kazmi, R., 2004. Quasi-static and dynamic loading responses and constitutive modeling of titanium alloys. Int. J. Plasticity 20, 2233–2248.
Liu, Y., Wu, X., 2006. An electron-backscattered diffraction study of the texture evolution in a coarse-grained AZ31 magnesium alloy deformed in tension at elevated temperatures. Metall. Mater. Trans. A 37, 7–17.
Lopes, A.B., Barlat, F., Gracio, J.J., Duarte, J.F., Rauch, E.F., 2003. Effect of texture and microstructure on strain hardening anisotropy for aluminum deformed in uniaxial tension and simple shear. Int. J. Plasticity 19, 1–22.
Lou, X.Y., Li, M., Boger, R.K., Agnew, S.R., Wagoner, R.H., 2007. Hardening evolution of AZ31B Mg sheet. Int. J. Plasticity 23, 44–86.
Mahajan, S., Williams, D.F., 1973. Deformation twinning in metals and alloys. Int. Metall. Rev. 18, 43–61.
Maksoud, I.A., Ahmed, H., Rödel, J., 2009. Investigation of the effect of strain rate and temperature on the deformability and microstructure evolution of AZ31 magnesium alloy. Mater. Sci. Eng. A 504, 40–48.
Matthies, S., Wenk, H.-R., 1992. Optimization of texture measurements by pole figure coverage with hexagonal grids. Phys. Status Solidi A 133, 253–257.
Muránsky, O., Carr, D.G., Šittner, P., Oliver, E.C., 2009. In situ neutron diffraction investigation of deformation twinning and pseudoelastic-like behaviour of extruded AZ31 magnesium alloy. Int. J. Plasticity 25, 1107–1127.
Nave, M.D., Barnett, M.R., 2004. Microstructures and textures of pure magnesium deformed in plane-strain compression. Scripta Mater. 51, 881–885.
Nobre, J.P., Noster, U., Kommeier, M., Dias, A.M., Scholtes, B., 2002. Deformation asymmetry of AZ31 wrought magnesium alloy. Key Eng. Mater., 230–232.
Proust, G., Tomé, C.N., Jain, A., Agnew, S.R., 2009. Modeling the effect of twinning and detwinning during strain-path changes of magnesium alloy AZ31. Int. J. Plasticity 25, 861–880.
Rauch, E.F., 1998. Plastic anisotropy of sheet metals by simple shear tests. Mater. Sci. Eng. A 241, 179–183.
Reed-Hill, R.E., 1973. Role of deformation twinning in determining the mechanical properties of metals: the inhomogeneity of plastic deformation. Am. Soc. Metals 285, 311.
Reed-Hill, R.E., Abbaschian, R., 1994. Physical Metallurgy Principles. PWS Publishing Company, Boston.
Staroselsky, A., Anand, L., 2003. A constitutive model for hcp materials deforming by slip and twinning: application to magnesium alloy AZ31B. Int. J. Plasticity 19, 1843–1864.
Styczynski, A., Hartig, C., Bohlen, J., Letzig, D., 2004. Cold rolling textures in AZ31 wrought magnesium alloy. Scripta Mater. 50, 943–947.
Thuillier, S., Manach, P.Y., 2009. Comparison of the work-hardening of metallic sheets using tensile and shear strain paths. Int. J. Plasticity 25, 733–751.
Tozawa, Y., 1978. Plastic deformation behavior under conditions of combined stress. In: Koistinen, D.P., Wang, N.-M. (Eds.), Mechanics of Sheet Metal Forming. Plenum Press, New York, London.
Tucker, M.T., Horstemeyer, M.F., Gullett, P.M., Kadiri, H.El., Whittington, W.R., 2009. Anisotropic effects on the strain rate dependence of a wrought magnesium alloy. Scripta Mater. 60, 182–185.
Ulacia, I., Dudamell, N.V., Gálvez, F., Yi, S., Pérez-Prado, M.T., Hurtado, I., 2010. Mechanical behavior and microstructural evolution of a Mg AZ31 sheet at dynamic strain rates. Acta Mater. 58, 2988–2998.
Wack, B., Tourabi, A., 1993. Cyclic simple shear of metallic sheets: application to aluminium lithium alloy. J. Mater. Sci. 28, 4735–4743.
Watanabe, H., Tsutsui, H., Mukai, T., Kohzu, M., Tanabe, S., Higashi, K., 2001. Deformation mechanism in a coarse-grained Mg–Al–Zn alloy at elevated temperatures. Int. J. Plasticity 17, 387–397.
Yi, S.-B., Davies, C.H.J., Brokmeier, H.-G., Bolmaro, R.E., Kainer, K.U., Homeyer, J., 2006. Deformation and texture evolution in AZ31 magnesium alloy during uniaxial loading. Acta Mater. 54, 549–562.
Yukutake, E., Kaneko, J., Sugamata, M., 2003. Anisotropy and non-uniformity in plastic behavior of AZ31 Magnesium alloy plates. Mater. Trans. 44, 452–457.
Zhang, E., Yin, D., Xu, L., Yang, L., Yang, K., 2009. Microstructure, mechanical and corrosion properties and biocompatibility of Mg–Zn–Mn alloys for biomedical application. Mater. Sci. Eng. C 29, 987–993.